remote sensing

Article

The Evaluation of FY-3E Hyperspectral Infrared Atmospheric Sounder-II Long-Wave Temperature Sounding Channels

Jing Huang [1,2], Gang Ma [1,2,*], Guiqing Liu [1,2], Juan Li [1,2] and Hua Zhang [1,2]

[1] CMA Earth System Modeling and Prediction Centre (CEMC), China Meteorological Administration, Beijing 100081, China; huangj@cma.gov.cn (J.H.)
[2] State Key Laboratory of Severe Weather, China Meteorological Administration, Beijing 100081, China
* Correspondence: magang@cma.gov.cn

Abstract: Prior to assimilating hyperspectral infrared data on the FengYun (FY) satellite in the numerical weather prediction (NWP) system, it is necessary to identify the quality and bias characteristics of these data, especially as China's first early-morning-orbit satellite data. Using the numerical model CMA-GFS (China Meteorological Administration Global Forecast System) and the observation of FY-3E HIRAS-II (Hyperspectral Infrared Atmospheric Sounder-II), the differences between observed and simulated brightness temperatures (O-Bs) are comprehensively analyzed, with a focus on evaluating the long-wave (LW) temperature sounding channels of HIRAS-II observation in the clear sky. The results show that the O-Bs in the LW channels are between $\pm$1.0 K, except for the CO_2 absorption line peak at 667 cm^{-1}. Only a tiny variation in O-Bs, with relative consistency, could be observed during the day, the line of dawn and dusk, and night. The difference in the standard deviations of O-Bs in the three cases is less than 0.1 K. The O-Bs of two typical channels (channels 14 and 47) in the stratosphere have disturbances at individual times, whereas the O-Bs are much more stable in time series in the tropospheric channels. The O-Bs in different channels show the characteristics of changing with the latitude, but the bias and standard deviations of O-Bs during the ascending and descending stages are not much different, except for the bias of channel 47 in low latitude. The optimal ranking of Fields of View (FOVs) in assimilation is derived from a priori analysis of O-Bs. The results demonstrate that FOV4 and FOV5 are the best in a Field of Regard (FOR) compared to all LW channels of HIRAS-II in constructions of their O-Bs and magnitude of O-B standard deviations, and they can be used as the preferred FOVs for assimilation. While the O-Bs in FOV1 and FOV2 are slightly larger, the O-Bs' characteristics also meet the assimilation requirements and can be used as assimilation FOVs in HIRAS-II LW channels after FOV4 and FOV5 lose their efficacy.

Keywords: FengYun-3E satellite; Hyperspectral Infrared Atmospheric Sounder-II; data assimilation; bias characteristics

check for updates

Citation: Huang, J.; Ma, G.; Liu, G.; Li, J.; Zhang, H. The Evaluation of FY-3E Hyperspectral Infrared Atmospheric Sounder-II Long-Wave Temperature Sounding Channels. *Remote Sens.* **2023**, *15*, 5525. https://doi.org/10.3390/rs15235525

Academic Editors: Filomena Romano and Elisabetta Ricciardelli

Received: 27 October 2023
Revised: 21 November 2023
Accepted: 24 November 2023
Published: 27 November 2023

1. Introduction

Since the launch of the Atmospheric Infrared Sounder (AIRS) instrument onboard the Aqua satellite in 2002, hyperspectral infrared data have been widely used in operational numerical weather prediction (NWP) [1]. The assimilation of large quantities of satellite data is crucial for improving the forecast skill within NWP systems [1–3]. The operational experiences of the European Centre for Medium-Range Weather Forecasts (ECMWF) and the UK's Meteorological Office indicate that the assimilation of hyperspectral infrared data from satellite-borne sounders, such as AIRS, the Infrared Atmospheric Sounding Interferometer (IASI), and the Cross-Track Infrared Sounder (CrIS), contributes the most to global numerical forecasts, as well as the microwave sounding data [1,4].

Hyperspectral sounders with spectral resolving power ($\lambda/\triangle\lambda$) greater than 1000 can provide high-vertical-resolution information on the temperature and humidity profiles [5]. The AQUA/AIRS contains 2378 infrared channels, with a nominal spectral resolving power

$\lambda/\triangle\lambda = 1200$. Under clear skies, the vertical resolution for temperature profiles can be up to 1 km [6]. Similar hyperspectral sounders include IASI with 8461 channels onboard the Metrological Operational (MetOp) satellites [7], CrIS with 2211 channels onboard the Suomi National Polar-Orbiting Partnership (SNPP) and the Joint Polar Satellite System (JPSS) [8], HIRAS with 2275 channels onboard FengYun-3D (FY-3D) satellite [9], and the Geostationary Interferometric Infrared Sounder (GIIRS) with 1650 channels onboard FengYun-4A (FY-4A) [10]. Starting from the launch of the Earth Observing System (EOS)/AQUA satellite, the Atmospheric Infrared Sounder (AIRS), along with the Advanced Microwave Sounding Unit (AMSU), forms an advanced high-vertical-resolution sounding system under clear and cloudy conditions [11].

New satellites and sensors from the launch stage to data operational applications need to undergo a series of tests and evaluations, such as a spectral radiometric calibration and uncertainty analysis, to ensure the quality of observation data [12]. The bias analysis of observation minus simulation based on the global numerical prediction models is an important process for the calibration and validation of satellite observation data [13]. Compared to the traditional broadband infrared detectors that use filters to separate light, the structure of hyperspectral infrared sounders is more complex. From instrument design and manufacturing in the laboratory to on-orbit testing during satellite launch, more simulation validation is required before the corresponding impact of data assimilation can be reflected in numerical prediction models [14–16]. HIRAS is China's first-generation satellite-borne hyperspectral infrared sounder, which was launched in 2017 and put into operation in the same year on the FY-3D satellite in afternoon orbit [17]. For the evaluation of HIRAS data, there are on-orbit performance assessments of the radiometric calibration [18] and data quality assessments based on the difference between observation and simulation [19]. These studies indicate the overall good consistency of the observation accuracy between HIRAS and IASI, CrIS. By comparing the biases of the four FOVs in HIRAS, it is pointed out that the standard deviation of FOV3 is greater than that of other FOVs [19].

The FY-3E satellite was successfully launched on 5 July 2021, and it is China's first early-morning-orbit meteorological satellite [20]. HIRAS-II is the second-generation satellite-borne hyperspectral infrared sounder onboard FY-3E, focusing on some upgrades from FY-3D HIRAS, such as the sensitivity of the detector, the accuracy of spectral calibration and radiometric calibration [21]. Zhang et al. [22] evaluated the radiometric calibration accuracy of HIRAS-II based on the bias of O-B and compared it with MetOp-C/IASI, and they found that the double difference between the two instrument data in most channels was better than 1 K. The study [22] focused on assessing the accuracy of radiometric calibration, using on-orbit test data, while this paper primarily evaluates the assimilation-oriented bias characteristics, using more officially released data. The optimal FOVs within each FOR are especially recommended for the operational data assimilation system.

In this paper, the evaluation focuses on the bias characteristics of HIRAS-II temperature sounding channels in a clear sky. The observations are from the officially released HIRAS-II L1 data (http://data.nsmc.org.cn, accessed on 10 April 2023). The CMA-GFS 6 h forecast field is used as input for the radiative transfer model RTTOV (Radiative Transfer for TOVS) to simulate the HIRAS-II brightness temperature. By analyzing the bias characteristics in LW channels, the preferred FOVs and secondary FOVs are determined for assimilation, and they also provide a reference for bias correction and channel selection. The remainder of this paper is organized as follows: Section 2 briefly introduces HIRAS-II observations and numerical prediction models. Data preprocessing and quality control are described in Section 3. Section 4 presents the O-B analysis results, including the consistency of each FOV and the variation in bias regarding the scanning position, latitude, and orbit location. The diurnal variation in bias is also described here. Finally, conclusions are given in Section 5.

2. Materials

2.1. CMA-GFS Model and Evaluation Method

CMA-GFS is the operational global numerical prediction system of the China Meteorological Administration. The main components include four-dimensional variational (4D-Var) data assimilation; a semi-implicit semi-Lagrangian temporal integration scheme and fully compressible non-hydrostatic equations of motion on the sphere; a modularized model physics package; and the data assimilation and prediction systems for global/regional integration [23,24]. The CMA-GFS model has 87 vertical layers, with the top pressure being approximately 0.1 hPa. The 4D-Var variational assimilation system applies an incremental analysis scheme, with horizontal resolutions of 1.0 degrees and 0.25 degrees in the inner and outer circulation, respectively [25]. The forward operator for satellite data assimilation is the fast radiative transfer mode RTTOV v12 developed by NWP SAF (EUMETSAT Satellite Applications Facility for NWP) [26]. The 4D-Var system can assimilate multi-source observations, with a 6 h assimilation time window being split into 30-min time slots, including radiosonde data, surface synoptic data, aircraft reports, ship reports, atmospheric motion vectors, Global Navigation Satellite System radio occultation sounder data, microwave temperature-sounder data, microwave humidity-sounder data, hyperspectral infrared data, microwave radiation imager data, scatterometer wind data, etc. In this paper, the CMA-GFS 6 h global forecast fields from 18 February to 4 March 2023 are used as input for the RTTOV in the experiment to simulate the brightness temperature of HIRAS-II.

The O-B bias (Bias) and standard deviation (Std) were used as the metrics to evaluate the data quality. The two metrics can be calculated as follows:

$$\mathrm{Bias_{jmean}} = \frac{1}{\mathrm{N}}\sum_{\mathrm{i}=1}^{\mathrm{N}} \left(\mathrm{O_{ij}} - \mathrm{B_{ij}}\right) \tag{1}$$

$$\mathrm{Std_j} = \sqrt{\frac{1}{\mathrm{N}-1}\sum_{i=1}^{\mathrm{N}} \left(\mathrm{Bias_{ij}} - \mathrm{Bias_{jmean}}\right)^2} \tag{2}$$

where N denotes the total number of observations, j denotes the channel, $\mathrm{O_{ij}}$ is the ith observed brightness temperature in channel j, $\mathrm{B_{ij}}$ is the corresponding simulated brightness temperature, $\mathrm{Bias_{jmean}}$ represents the mean bias of the jth channel, and $\mathrm{Std_j}$ is the standard deviation of the jth channel. Bias represents the difference between the observed and simulated brightness temperature; Std represents the degree of spread between individual samples.

2.2. HIRAS-II Observations

HIRAS-II carried on FY-3E is an interferometric Fourier-transform spectrometer that observes the upwelling infrared radiation within a spectral range of 650 to 2550 $\mathrm{cm^{-1}}$ at the top of the atmosphere. The instrument's working spectrum is divided into three infrared spectral bands: long wave (LW, 650~1168.125 $\mathrm{cm^{-1}}$), medium wave (MW, 1168.75~1920 $\mathrm{cm^{-1}}$), and short wave (SW, 1920.625~2550 $\mathrm{cm^{-1}}$), with a spectral resolution of 0.625 $\mathrm{cm^{-1}}$ and a total of 3041 channels with an apodized spectral resolution. HIRAS-II views the ground in a cross-orbit scanning manner, and in each scan line, there are 32 Fields of Regard (FORs), including 28 continuous Earth targets, 2 cold space targets, and 2 blackbody observation targets. Each Field of Regard (FOR) comprises a 3 × 3 array of Fields of View (FOVs), corresponding to an FOV of approximately 14 km resolution at the nadir. In this paper, we mainly select spectral channel data between LW 651.25 $\mathrm{cm^{-1}}$ and 746 $\mathrm{cm^{-1}}$ for analysis, which is located in the CO_2 absorption line and distributed on both sides of the 667 $\mathrm{cm^{-1}}$ CO_2 absorption peak (hereinafter referred to as "absorption peak"), and the vertical detection of atmospheric temperature from 5 hPa to 1000 hPa can be achieved, as shown in Figure 1.

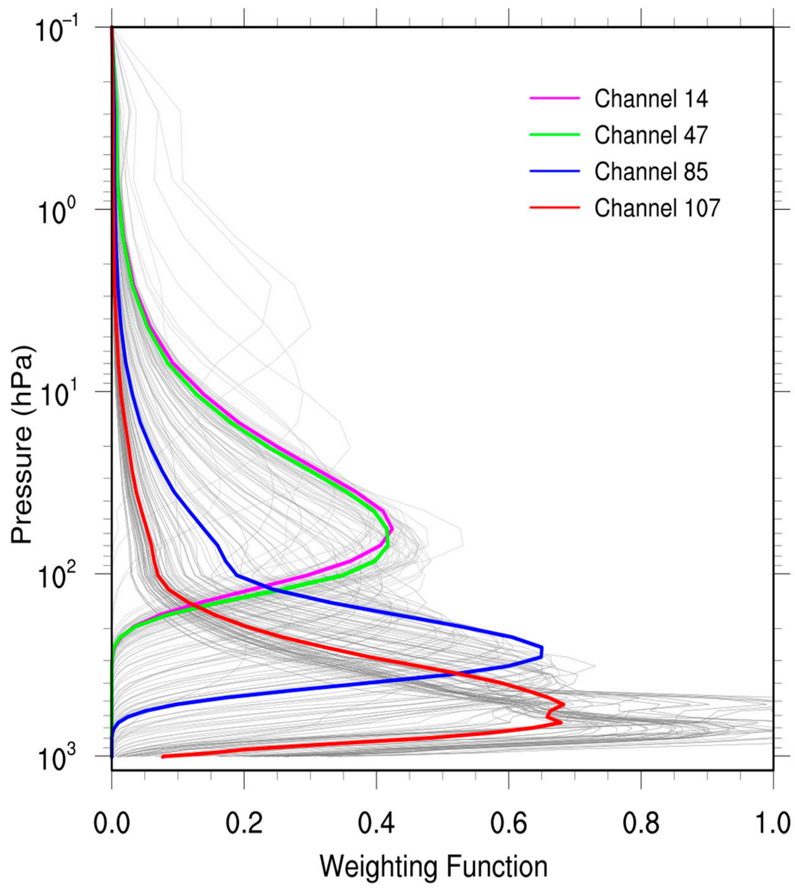

Figure 1. Weighting function for channels at 651.25~746 cm^{-1} of FY-3E HIRAS-II.

In this paper, we select channel 14 (658.125 cm^{-1}) and channel 47 (678.75 cm^{-1}) in the stratosphere, channel 85 in the upper troposphere (at 702.5 cm^{-1}) and channel 107 in the middle troposphere (at 716.25 cm^{-1}) to conduct an intensive O-B analysis. The NEΔT (Noise Equivalent Differential Temperature) varies from 0.8 K to 0.2 K across the 667 cm^{-1} band from longer to shorter wavelengths in the analyzed band, respectively (https://space.oscar.wmo.int/instruments/view/hiras_2, accessed on 9 November 2023).

3. Data Processing Method

3.1. Data Preprocessing of HIRAS-II

For a comparison with the forward model, the apodized spectrum is used. The Hamming apodization function with a three-point filter (0.23, 0.54, and 0.23) of the running mean is performed [27]. After the apodization, the brightness temperatures for the HIRAS-II channels are calculated from radiances data by Planck's blackbody radiation law [27]. Figure 2 shows the average spectral brightness temperature for each channel of HIRAS-II over the mid- and low-latitude ocean before/after apodization on 25 February 2023. Figure 2a shows the full-spectrum brightness temperature, and the yellow area in the figure represents the LW CO_2 band analyzed in this paper. Figure 2b represents the brightness temperature of LW (651.25~746 cm^{-1}) in Figure 2a. After applying apodization in the entire spectrum, the side-lobes are effectively suppressed, and the spectrum becomes smoother.

3.2. Quality Control of HIRAS-II Data

Infrared radiation is strongly absorbed by cloud water particles, making it impossible to detect the atmospheric state under clouds. In order to avoid the uncertainties on cloudy-sky pixels, only clear-sky pixels of HIRAS-II were used. We used the clear channels scheme developed by McNally [28] for cloud detection. Based on the difference between the observed and simulated brightness temperature (O-B), this scheme selects clear channels that are not affected by clouds according to the sensitivity of the channels to clouds. Compared to traditional clear locations' cloud detection scheme [29], it increases the number of satellite data available for assimilation in cloudy areas. McNally's clear-channel scheme was applied for cloud detection in hyperspectral infrared data at ECMWF [30,31] and the Earth System Numerical Prediction Center of the China Meteorological Administration [32], and it was used successfully by these centers.

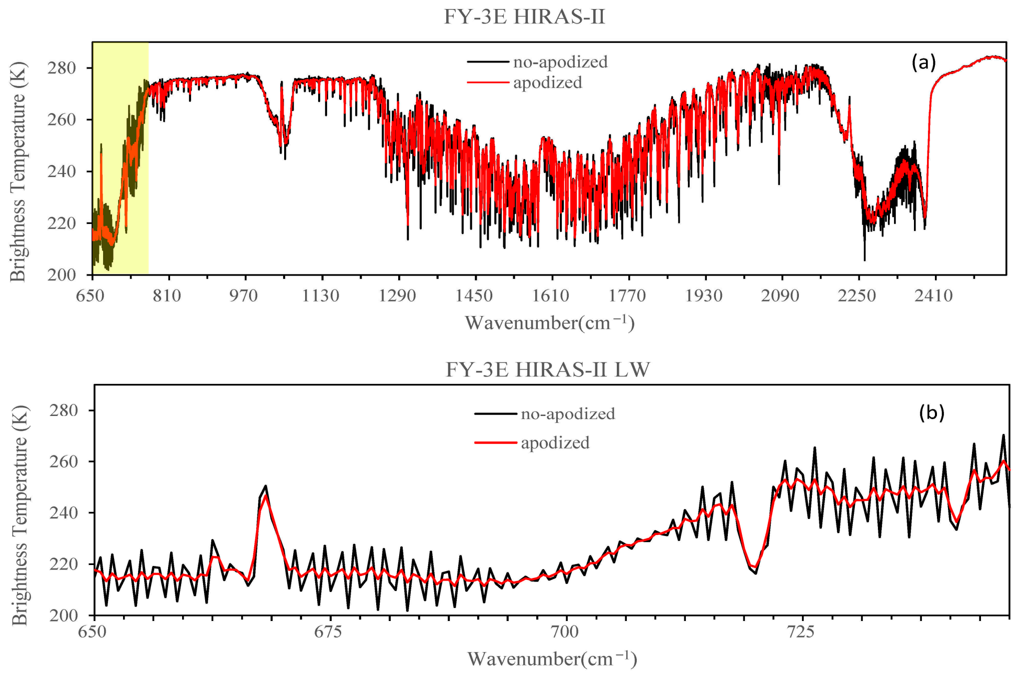

Figure 2. (**a**) Full-spectrum brightness temperature and (**b**) LW-spectrum brightness temperature before/after apodization on 25 February 2023.

Data with large deviations can also affect the accuracy of assimilation. As the data quality evaluation in this paper is oriented toward the data assimilation of numerical models, quality-controlled clear-sky data over the ocean are used for the statistical analysis. In addition to cloud detection, quality control also includes (1) removing values of observed brightness temperature exceeding the range of 150–350 K; (2) removing observations over complex terrains, such as land and coastline; (3) removing observations over sea ice, where the ocean surface temperature is below 271.45 K; (4) excluding observed brightness temperatures with residual errors greater than 4 K or observation residual greater than 3.0 times σ (σ is observation error). Figure 3 shows the distribution of quality-controlled clear-sky pixels during 0300–0900 UTC on 25 February 2023, with the gray-scale image in the figure showing the brightness temperature of window channel 444 (wavelength 10.79 µm). The light gray is cold, and the dark gray is hot, which can be considered a clear sky. The colorscaled pixels are the O-B (K) in channel 107 (the weight function peak is approximately 520 hPa) after cloud detection and quality control. It can be seen that the distribution of pixels in channel 107 over the ocean is not in the light gray area, and the cloud-contaminated pixels are effectively eliminated.

Figure 4 shows the comparison of observed and simulated brightness temperatures before/after cloud detection and quality control. The black dots in the figure represent O-B samples without cloud detection and quality control, while the red dots represent O-B samples applied with cloud detection and quality control. Figure 4a,b are the O-B distributions of channels 14 and 47, respectively, and their weight function peaks are above 100 hPa. The observed and simulated channel brightness temperatures show a high degree of consistency, with less data rejection of the upper channels by cloud detection and quality control. Figure 4c,d show that channels 85 and 107 (with detection heights below 250 hPa, as shown in Figure 1) are greatly affected by clouds, and the simulated brightness temperature differs greatly from some actual observations. After cloud detection and quality control, these observation data with abnormally large values of O-B were removed, and the observed and simulated brightness temperatures were within a ±1.6 K difference.

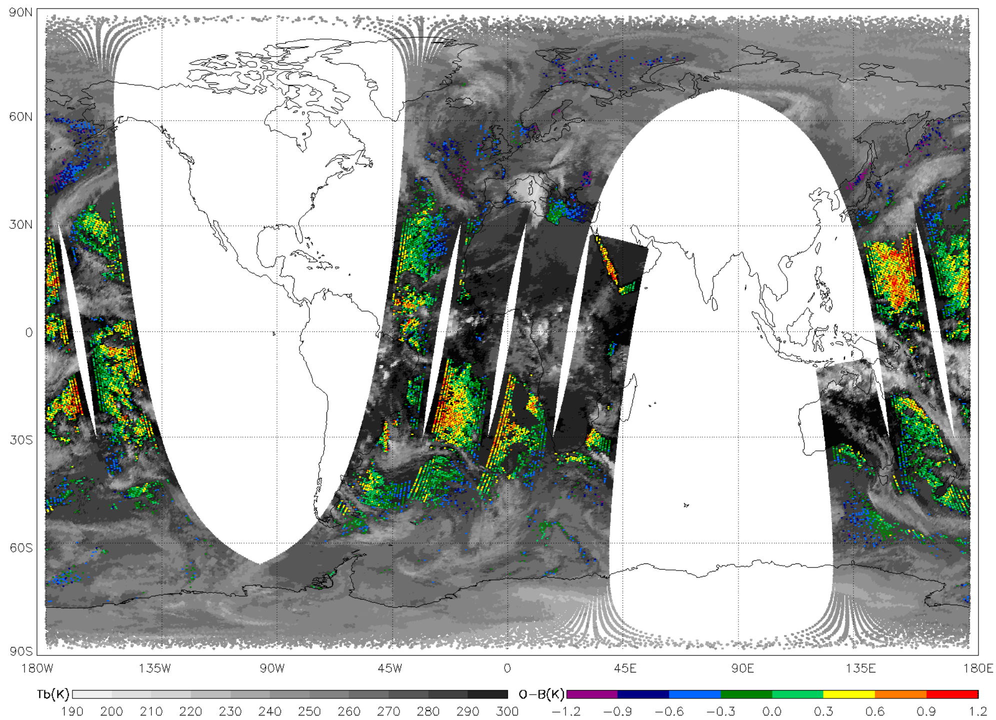

Figure 3. Comparison of quality-controlled clear-sky O-B global distribution in channel 107 and brightness temperature in channel 444 during 0300–0900 UTC on 25 February 2023.

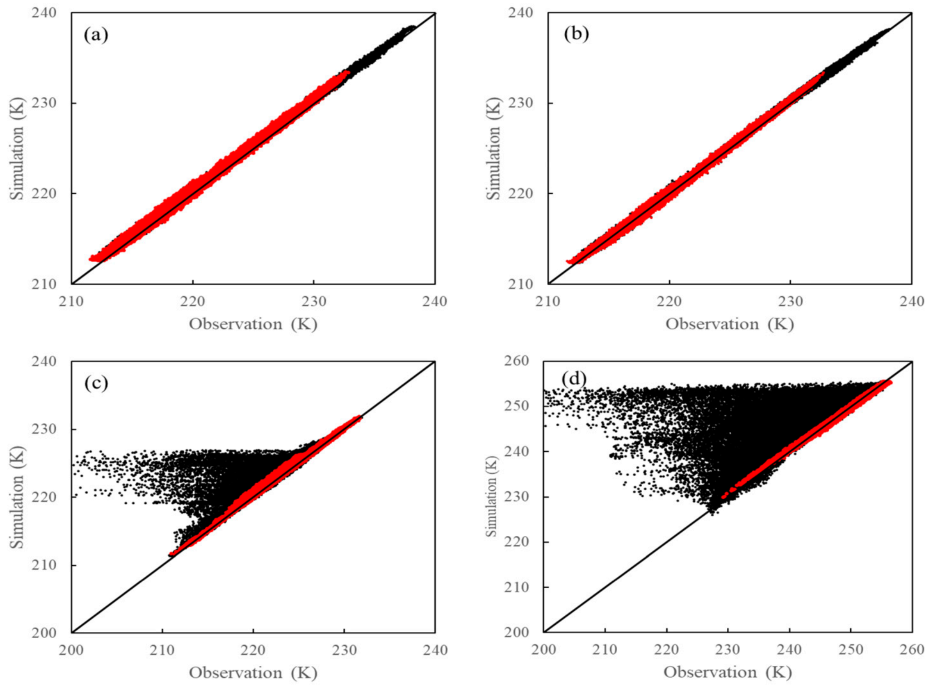

Figure 4. Comparison of observed (*x*-axis) and simulated (*y*-axis) brightness temperature at (**a**) channel 14, (**b**) channel 47, (**c**) channel 85, and (**d**) channel 107 during 0300–0900 UTC on 25 February 2023 (black dots, before quality control; red dots, after quality control and cloud detection).

4. Results

4.1. Analysis the Consistency of Each FOV

The O-B bias and standard deviation of each FOV for the 150 sequential channels were calculated by using data from 18 February to 4 March 2023 (Figure 5).

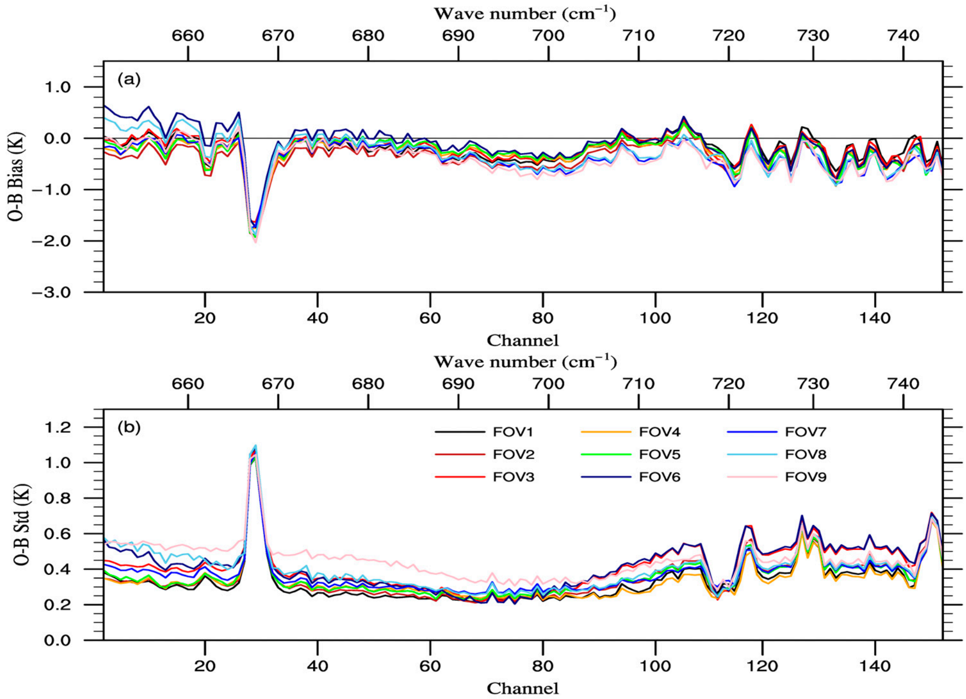

Figure 5. (**a**) O-B bias (Bias; units, K) and (**b**) standard deviation (Std; unit, K) at the LW channels of HIRAS-II FOV1-FOV9.

In Figure 5a, the average biases in the channels on the left side of 667 cm^{-1} absorption line exhibit significant discreteness with the change in FOV, for instance, the difference between the average biases of FOV2 and FOV6 at channel 9 (655 cm^{-1}) is about 0.7 K. In the absorption peak spectrum range of 667~670 cm^{-1}, O-B biases rapidly increase to about −2.0 K, which is much greater than the average biases between ±1.0 K in the wing region. The O-Bs in the channels (670~719 cm^{-1}) on the right side of the absorption line vary between −0.6 and 0.4 K; the O-Bs in the 720~746 cm^{-1} band show more of a fluctuation. Overall, the O-B bias of the LW spectrum, except for the absorption peak, is between ±1.0 K.

Figure 5b shows the variation in the O-B standard deviation with the spectrum, with the maximum standard deviation of 1.1 K near the CO_2 absorption peak being at 667 cm^{-1} for all FOVs. The standard deviation of all FOVs is the closest, and the value is the smallest in the 670.625~705 cm^{-1} spectral band, which is less than 0.4 K (excluding FOV9). In the 705~746 cm^{-1} band, the differences of the standard deviation in each channel among FOVs increases. There are small standard deviations in FOV1 in the spectral band on the left and right sides of the 667 cm^{-1} absorption peak of approximately 0.2–0.6 K for most channels. The standard deviation of FOV2 is distributed similarly to that of FOV1, but it is slightly larger than FOV1. The standard deviation of FOV3 on the left side of the absorption peak is 0.4 K, and it is the largest of the nine FOVs on the right side of 705 cm^{-1}. The O-B standard deviation of FOV3 varies significantly with the spectrum and cannot be used as a representative FOV for the assimilation of HIRAS-II observations. The standard deviations of FOV4 and FOV5 exhibit a similar distribution and do not show significant differences with spectral changes. Moreover, their standard deviations in most channels are stable between 0.2 and 0.55 K, which can also serve as representative FOVs for the assimilation of HIRAS-II observations. The variation characteristics in the standard deviation of FOV6 are similar to that of FOV3, and the O-B standard deviation changes significantly with the spectrum. The standard deviation of FOV7 on the left side of the absorption peak is about 0.4 K, while it is stable, with little change, on the right side; FOV8 shows a similar variation, but the maximum standard deviation on the left side of the absorption peak is greater than 0.5 K. The standard deviations of FOV9 in channels on the left side of 705 cm^{-1} are significantly greater than those of other FOVs. Considering the little variation of the standard deviation with the spectrum, FOV1, FOV2, FOV4, FOV5, and FOV7 can all be used as representative FOV observations for the assimilation of HIRAS-II.

Under clear-sky conditions, considering the bias consistency of FOVs is a necessary means to select representative FOVs for the assimilation of HIRAS-II data. Figure 6 shows the variation in the differences between the O-Bs for each FOV and the other eight FOVs in a FOR with channels. Figure 6a shows the comparison between FOV1 and the other eight FOVs. It can be seen that the average differences between the bias of FOV1 and that of the other FOVs in channels on the left side of the absorption peak are about 0.01 K, while the difference on the right is about −0.1 K. The difference between the bias of FOV1 and that of FOV2 (brown line) is the second largest on the left side of 690 cm^{-1}, with a value of −0.35 K at 653 cm^{-1}. As the wave number increases, the difference gradually decreases, and the difference becomes less than −0.2 K. The average difference between the biases of FOV1 and FOV3 (red line) within the LW spectral range is less than ±0.1 K, demonstrating good consistency. The differences between the biases of FOV1 and FOV4 (orange line) and FOV5 (green line) are less than −0.15 K in the channels on the left side of the absorption peak, making them slightly greater than the difference between FOV1 and FOV3. As the channel spectrum exceeds 710 cm^{-1}, the difference perturbs around −0.1 K, also indicating a good consistency. The difference between the biases of FOV1 and FOV6 (deep blue line) is the largest on the left side of 700 cm^{-1}, with a maximum value of 0.6 K (at 651.25 cm^{-1}), and approximately −0.1 K on the right side of 710 cm^{-1}. The maximum difference between the biases of FOV1 and FOV7 (sky blue line) and FOV9 (pink line) at the left channel of the absorption peak is less than −0.2 K, but at the channel to the right of 690 cm^{-1}, the difference between the biases increases to -0.4 K. The maximum difference between the biases of FOV1 and FOV8 (light blue line) on the left side of the absorption peak is 0.37 K. In the channel on the right side of the absorption peak, the difference between the biases is similar to that of FOV7 and FOV9.

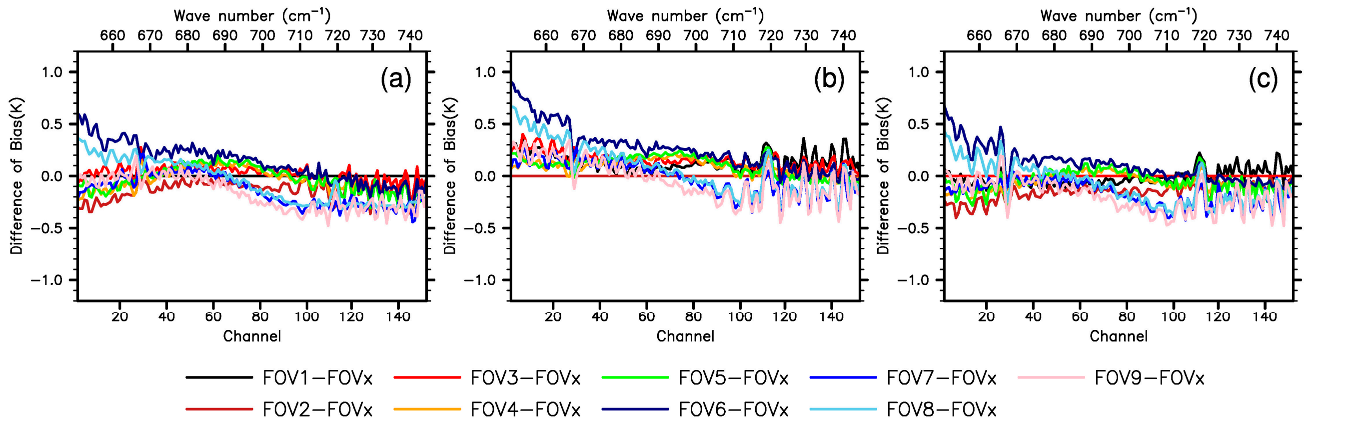

Figure 6. Comparison of the bias difference between one FOV and other FOVs (x in figure (**a**–**c**) represents 1–3, respectively). (**a**) Difference between the bias of FOV1 and that of other FOVs, (**b**) between FOV2 and other FOVs, and (**c**) between FOV3 and other FOVs.

Figure 6b shows the comparison between FOV2 and the other eight FOVs. It can be seen that the average bias difference in the left channels of the absorption peak is about 0.28 K, and in the right channels, it is about 0.15 K (excluding FOV7-9). The difference between the bias (black line) of FOV2 and FOV1 is distributed similarly to the brown line in

Figure 6a, but symmetrically along the x-axis. The difference between the bias of FOV2 and that of FOV3 (red line) reaches a maximum of 0.4 K in the left channels of the absorption line, while the average value in the right channels is 0.1 K. The differences between FOV2 and FOV4 (orange line) and FOV5 (green line) in the LW spectral range are less than 0.2 K, showing good consistency. The difference between FOV2 and FOV6 (dark blue line) is the largest on the left side of 700 cm^{-1}, with a maximum value of 0.9 K (at 651 cm^{-1}), and the difference on the right side of 700 cm^{-1} decreases with the increasing wavenumber. The differences between the biases of FOV2 and FOV7 (sky blue line) and FOV9 (pink line) are slightly smaller than the overall average on the left side of 700 cm^{-1}, but they are significantly increased on the right side, with a large amplitude at 720 cm^{-1}. The bias difference between FOV2 and FOV8 (light blue line) is greater than the average on the left side of 700 cm^{-1}, 0.7 K at 651 cm^{-1}, and the distribution and value of bias difference in the right channels of 700 cm^{-1} are very close to the sky-blue line.

Figure 6c shows the comparison between FOV3 and the other eight FOVs, and it can be seen that the average bias difference in the LW spectrum is about −0.1 K. The bias comparison (black line) between FOV3 and FOV1 is similar to the distribution of the red line in Figure 6a, but it is symmetrically distributed along the x-axis, showing good consistency. The analysis for the bias difference between FOV3 and FOV2 (brown line) is the same as the red line in Figure 6b. The differences between FOV3 and FOV4 (orange line) and FOV5 (green line) are about −0.15 K in the left channels of the absorption line and −0.1 K in the right, respectively, showing good consistency. The bias difference between FOV3 and FOV6 (dark blue line) is 0.65 K on the left side of 700 cm^{-1}, and then it decreases with the increase in the spectral wavenumber and remains around −0.1 K to the right side of 710 cm^{-1}. The distribution of bias difference between FOV3 and FOV7 (sky blue line) is similar to that of FOV3 and FOV9 (pink line), and the average bias difference in the left channels of 700 cm^{-1} is less than −0.2 K, while the right increases to −0.3 K. The bias difference between FOV3 and FOV8 (light blue line) is about 0.4 K on the left side of 700 cm^{-1}, and the distribution on the right is similar to the sky-blue line and pink line.

Figure 7 is similar to Figure 6, except that the bias differences of the other FOVs are compared to those of FOV4–6. Figure 7a shows the comparison of the other eight FOVs with FOV4, and the distributions of the bias differences of FOV4 and FOV1 (black line), FOV2 (brown line), and FOV3 (red line) are similar to the orange lines in Figure 6a–c, respectively, all of which are symmetrically distributed along the x-axis; in addition, the analysis conclusions are the same. In the right channels of the absorption peak, the average difference is less than −0.05 K. The difference between the bias of FOV4 and and that of FOV5 (green line) has good spectral stability in LW and fluctuates near the zero line, showing good consistency. The average bias difference between FOV4 and FOV6 (dark blue line) has a maximum value of about 0.85 K at 651.25 cm^{-1}; it then decreases to 0.1 K (at 700 cm^{-1}) and keeps stable in the remaining spectral channels of LW. The bias differences between FOV4 and FOV7 (sky blue line), FOV9 (pink line), and FOV8 (light blue line) tend to be consistent on the right side of the absorption peak, with the maximum value of about −0.4 K, but on the left side of the absorption peak, the difference with FOV8 is greatest; the maximum value is about 0.6 K.

Figure 7b shows the comparison of FOV5 with the other eight FOVs, and it can be seen that the differences between the biases at the left side of the absorption peak perturbate between −0.2 and 0.25 K (excluding FOV6 and FOV8). The conclusions of the distributions of bias difference from FOV5 to the first four FOVs are the same as those in Figures 6 and 7a. The maximum average difference between the bias of FOV5 and that of FOV6 (dark blue line) is about 0.7 K, occurring at 651.25 cm^{-1}, and then it decreases to 0.1 K (at 700 cm^{-1}) and remains stable in the remaining spectral channel of LW. On the left side of the absorption peak, the maximum difference between FOV5 and FOV8 (light blue line) is 0.45 K, and the maximum differences between FOV5 and FOV7 (sky blue line), and FOV9 (pink line) are both 0.2 K; while on the right side, the distributions of bias difference between FOV5 and FOV7–9 are similar.

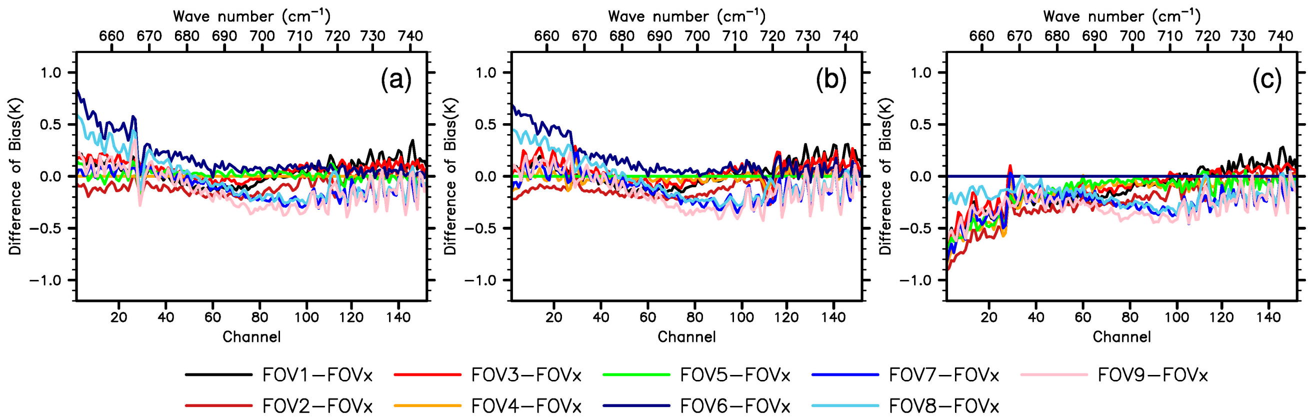

Figure 7. Similar to Figure 6, but for comparison with (**a**) FOV4, (**b**) FOV5, and (**c**) FOV6, respectively.

Figure 7c shows the comparison of FOV6 with the other eight FOVs, and it can be seen that the difference between the biases in the left channels of the absorption peak is about −0.4 K on average, and it is about −0.2 K in the right channels. The distribution of the bias difference between FOV6 and FOV7 (sky blue line) is similar to that between FOV6 and FOV9 (pink line), with the maximum average difference between the biases being in the left channels of 700 cm^{-1}; the maximum average is −0.65 K at 651.25 cm^{-1}, and that in the right of 700 cm^{-1} is about −0.25 K. The bias difference between FOV6 and FOV8 (light blue line) is maintained at about −0.2 K in the LW spectral range.

Figure 8 is similar to Figure 6, except that the other FOVs are compared to FOV7–9. Figure 8a exhibits the comparison of FOV7 to the other eight FOVs, and it can be seen that the average bias difference is about 0.2 K in the LW spectral range. The bias difference between FOV7 and FOV8 (light blue line) has a maximum of 0.53 K on the left side of 680 cm^{-1}, and it is stable at about 0 K on the right side. The bias difference between FOV7 and FOV9 (pink line) is stable between −0.1 K and 0.2 K in the LW spectral range (except in the vicinity of the absorption peak). Figure 8b compares FOV8 with the other eight FOVs, and it can be seen that the average bias differences of the left and right channels of the absorption peak are about −0.3 K and 0.1 K, respectively. The difference between the bias of FOV8 and that of FOV9 (pink line) is −0.38 K on the left side of 667 cm^{-1}, while on the right side of 667 cm^{-1}, it is stable at about −0.1 K. Figure 8c compares FOV9 with the other eight FOVs, and it can be seen that the bias difference in many channels exceeds 0.4 K.

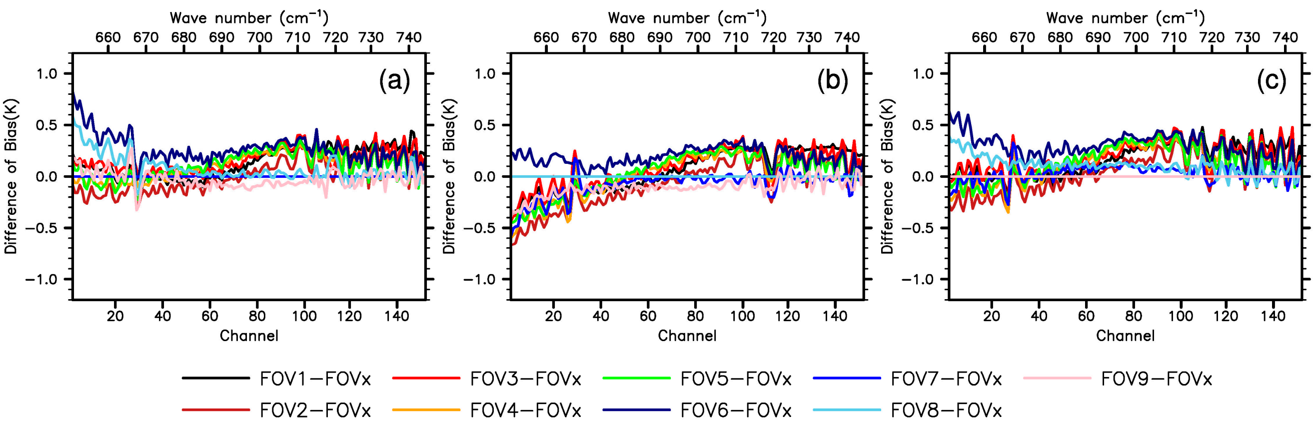

Figure 8. Similar to Figure 6, but for comparison with (**a**) FOV7, (**b**) FOV8, and (**c**) FOV9, respectively.

Based on the above analysis, the O-B biases of FOV4–5 and other FOVs have a high degree of consistency in the LW spectral range, the biases of FOV1–2 and other FOVs show secondary consistency, and the biases of the remaining FOVs (excluding FOV1–2 and FOV4–5) and other FOVs in FOR have a relatively large change with spectrum in many cases.

4.2. Variation in Bias with Scan Position

Within each FOR of FY-3E HIRAS-II, the FOV 5 is the center FOV. In a scan line, the position of other FOVs rotates around the center FOV. There are 28 continuous FORs in one scan line of HIRAS-II. The area projected on the surface of the Earth of FOR and FOV increases with the corresponding scan angle. The horizontal resolution of the HIRAS-II FOV is the largest at the nadir and is the smallest at the edge of the scan.

Figure 9 shows the change in the average O-B bias in nine FOVs in channels 14, 47, 85, and 107 with FOR numbers from 18 February to 4 March 2023. It can be seen that the biases in FOV1 and FOV4 are stable and basically do not change with the scanning position. The distribution of bias in FOV7 shows a high degree of symmetry with the nadir as the midpoint. The biases in FOV2, FOV3, FOV5, and FOV6 are distributed similarly, showing monotonic quasilinear changes with the increase in the scanning points, in which the biases of the tropospheric channel and stratospheric channels in FOV3 and FOV6 evolve in the reverse phase, and the variation amplitudes of biases with the scanning position are greater than those in FOV2 and FOV5. The increment/decrement of biases in FOV8 and FOV9 with the change in scanning position is monotonic and nonlinear, and it is numerically larger than other FOVs. In general, the biases of the two stratospheric channels are close, and their trends are consistent with the change in FOR; in addition, the biases of the tropospheric channels on both sides of the scan line are greater than those of the stratosphere channels. Based on the above analysis, the observations of FOV1, FOV2, FOV4, and FOV5 can be used as representatives in the assimilation of HIRAS-II observation, but the asymmetric distribution of biases in the entire scan line in the observations of FOV2 and FOV5 should be considered in assimilation.

4.3. Diurnal Variation in Bias

We use the solar zenith angle as the basis to determine whether the observation data are daytime or nighttime data. When the solar zenith angle is less than 80°, the observations are considered to be the daytime samples; when the solar zenith angle is within 80°~90°, the observations are used as samples near the line of dawn and dusk; and when the solar zenith angle is greater than 90°, the observations are used as nighttime samples. Figure 10 shows the distribution of the O-B bias and standard deviation in three cases for the 5th FOV (FOV5) in 150 channels. The sample of the line of dawn and dusk has the largest negative bias on the left side of 690 cm^{-1}, and the difference between this negative bias and the O-B bias in the other two cases is less than 0.15 K, regardless of the absorption peak region (Figure 10a). In the spectrum channels to the right of 690 cm^{-1}, the negative bias during the day is the largest, and the maximum difference from the other two cases is 0.3 K. In the statistics of standard deviation in Figure 10b, the standard deviations of the three cases are basically the same to the left of 705 cm^{-1} (except in the vicinity of the absorption peak at 667 cm^{-1}); to the right of 705 cm^{-1}, the difference between O-B standard deviations in the three cases is less than 0.1 K, with the largest standard deviation being at the line of dawn and dusk and the smallest being during the day. In general, the differences between the O-B among HIRAS-II LW channels during the day, the line of dawn and dusk, and night are small, and the variations are relatively consistent. The distributions of O-B bias and standard deviation of other FOVs are similar to the distribution of FOV5, except for differences in the numerical value, and the analysis results are not shown here.

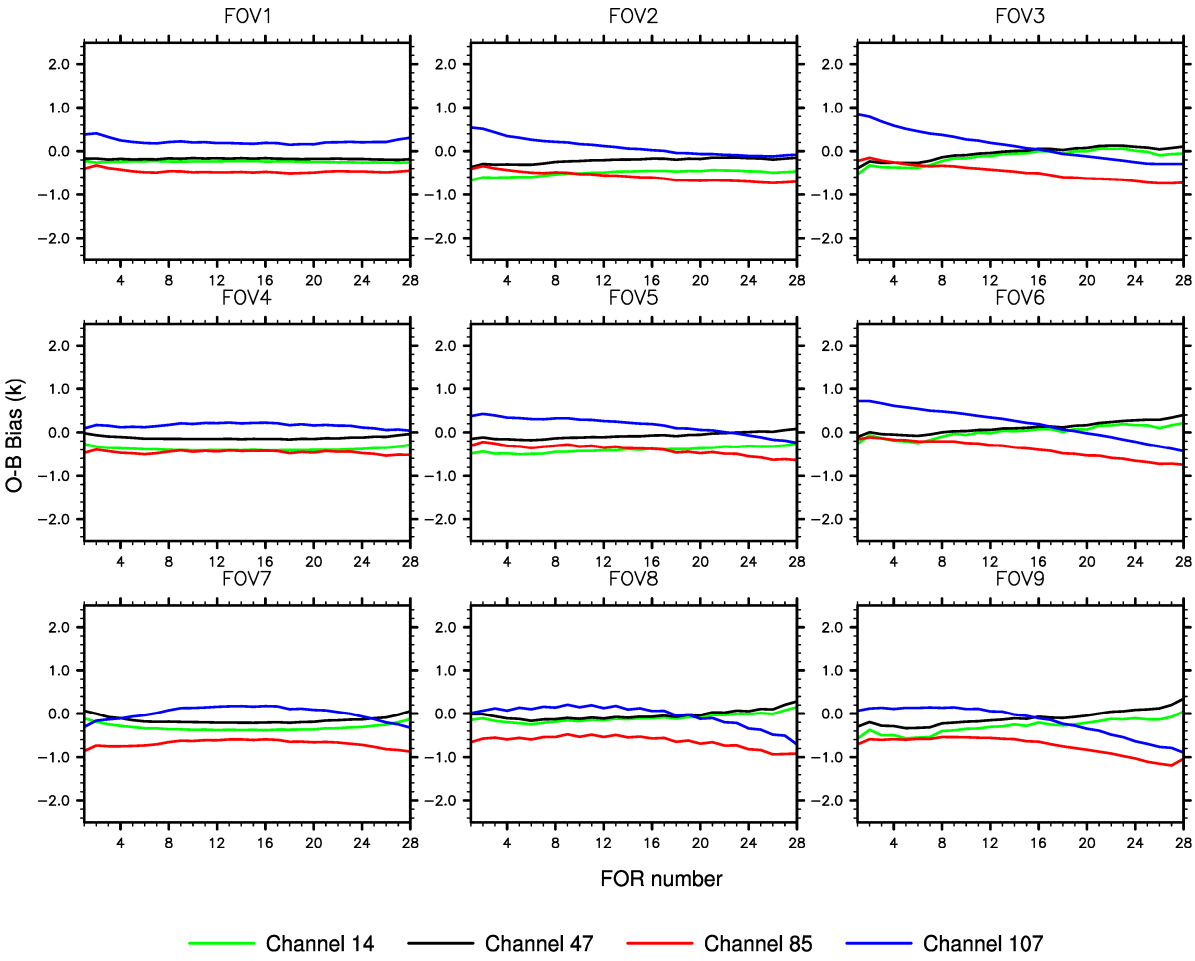

Figure 9. Change in the average O-B bias of the nine FOVs in channels 14, 47, 85, and 107 with FOR number from 18 February to 4 March 2023.

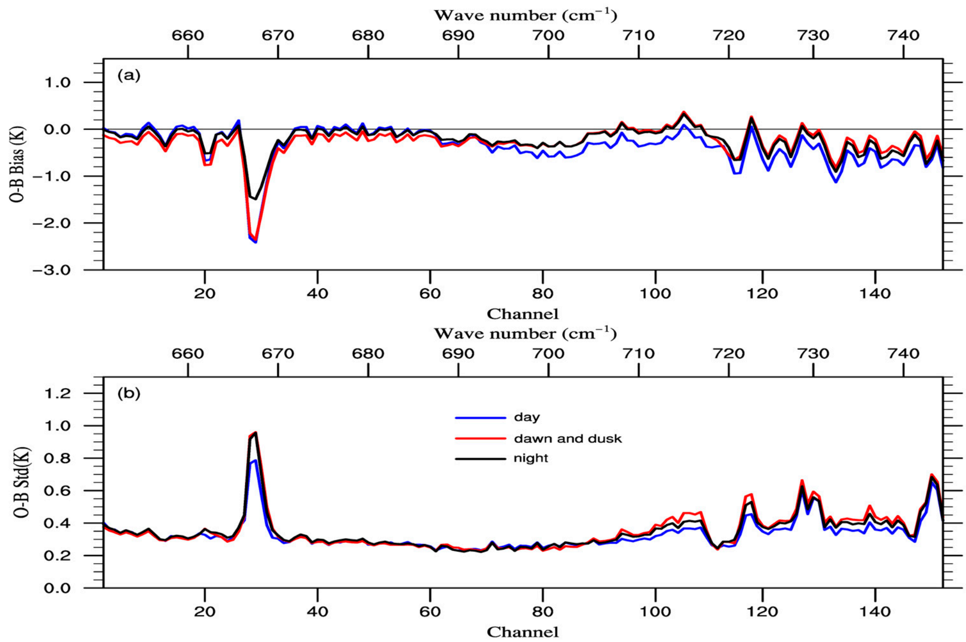

Figure 10. Distribution of the O-B (**a**) bias and (**b**) standard deviation in LW channels during the day and night.

Figure 11 shows the temporal variation in O-B bias and standard deviation for HIRAS-II channels 14, 47, 85, and 107. We can see that the O-B bias of channel 14 oscillates between −0.7 and −0.25 K (Figure 11a); the O-B bias of channel 47 is always less than −0.4 K, with a maximum value of −0.4 K at one time, and the standard deviation was stable at about 0.3 K (Figure 11b). Figure 11c is the O-B distribution of channel 85, the deviation is stable around −0.4 K during the whole statistical period, and the standard deviation is maintained at 0.3 K, with only a jitter of about 0.1 K occurring on 27 February; the O-B bias of channel 107 (Figure 11d) has a small jagged perturbation with the amplitude of about 0.1 K, and the average O-B bias and standard deviation are 0.2 K and 0.4 K, respectively. The above results show that the standard deviations of O-Bs of the four channels are basically unchanged with time, but the biases of the upper channels (channels 14 and 47) have disturbances at individual times, with similar variation characteristics with time, and the biases of the tropospheric channels are much more stable.

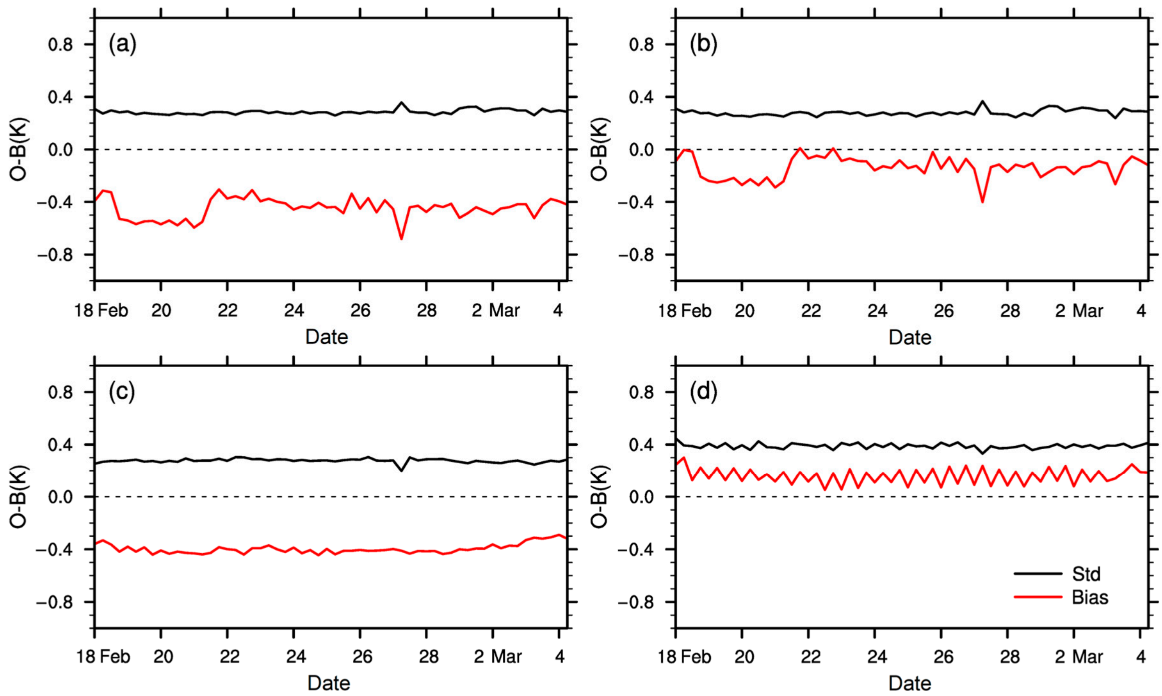

Figure 11. Time series of the O-B bias (red) and standard deviation (black) of FOV5 in LW channels (**a**) 14, (**b**) 47, (**c**) 85, and (**d**) 107 after quality control from 18 February to 4 March 2023.

4.4. Variation in Bias with Latitude and the Ascending/Descending Orbits

Previous studies have pointed out that scanning bias strongly varies with latitude [33,34]. In order to analyze the relationship between HIRAS-II bias and latitude bands, the statistical biases and standard deviations of channels 14, 47, 85, and 107 are plotted in 10° intervals in Figure 12 during the ascending and descending phases, respectively, where Figure 12a,c show the statistical biases of ascending and descending orbits, and Figure 12b,d are the corresponding standard deviations. It should be noted that there are few or even no samples with latitudes greater than 80°, so there is no statistical representativeness, and they are not plotted in Figure 12. Channel 107 reflects the distribution of temperature in the troposphere. As can be seen in Figure 12a, the bias of O-B changes in the range from −0.6 to 0.4 K, and it is positive between 30°N and 30°S, with a maximum value of about 0.4 K. As the latitude increases, the O-B bias gradually decreases to be negative at high latitudes, reaching a maximum negative value at the North Pole. The peak value of the weighting function in channel 85 is about 253 hPa. The bias of O-B in channel 85 is negative globally, with a value range from −0.6 to 0 K, and the maximum negative bias at low latitudes. As a stratospheric temperature detection channel, the O-B bias range of channel 47 is from

−0.5 to 0.1 K, positive between 20°S and 10°S, and negative in the rest of the region. It exhibits a negative bias in channel 14 globally, and the negative value is above −0.6 K in high latitudes in the Southern Hemisphere. In Figure 12c, the negative biases of upper channels 14 and 47 in the descending orbit stage are generally smaller than those in the ascending stage, and the relatively obvious difference is that channel 47 has a weak positive bias in the descending stage in the low latitude, while it has a weak negative bias in the corresponding ascending stage. The O-B bias distributions of tropospheric channels 85 and 107 are close to those in Figure 12a, with slight differences in the distribution in the latitude zone, and the bias differences between the ascending and descending orbits are less than 0.1 K. Figure 12b shows the distribution of O-B standard deviation for the four channels. The O-B standard deviation range of channel 107 is from 0.2 to 0.4 K, the maximum value is between the Equator and 30°N, and the standard deviation decreases with latitude. For channel 85, the standard deviation value range is 0.15 to 0.35 K, the maximum value is near the Equator, and the value decreases with latitude. The distributions of the O-B standard deviations in upper channels 14 and 47 are basically the same as those of other channels, but the value range is from 0.2 to 0.3 K. Figure 12d shows the distribution of the O-B standard deviation in the descending orbit stage, and the value range, maximum value, and distribution characteristics of O-Bs are similar to those in the ascending orbit, and the difference between the two stages is less than 0.05 K. In general, the O-Bs of different channels show the characteristics of changing with the latitude band, but the bias and standard deviation differences between the ascending and descending orbits are not much different (except for the bias of channel 47 in low latitude).

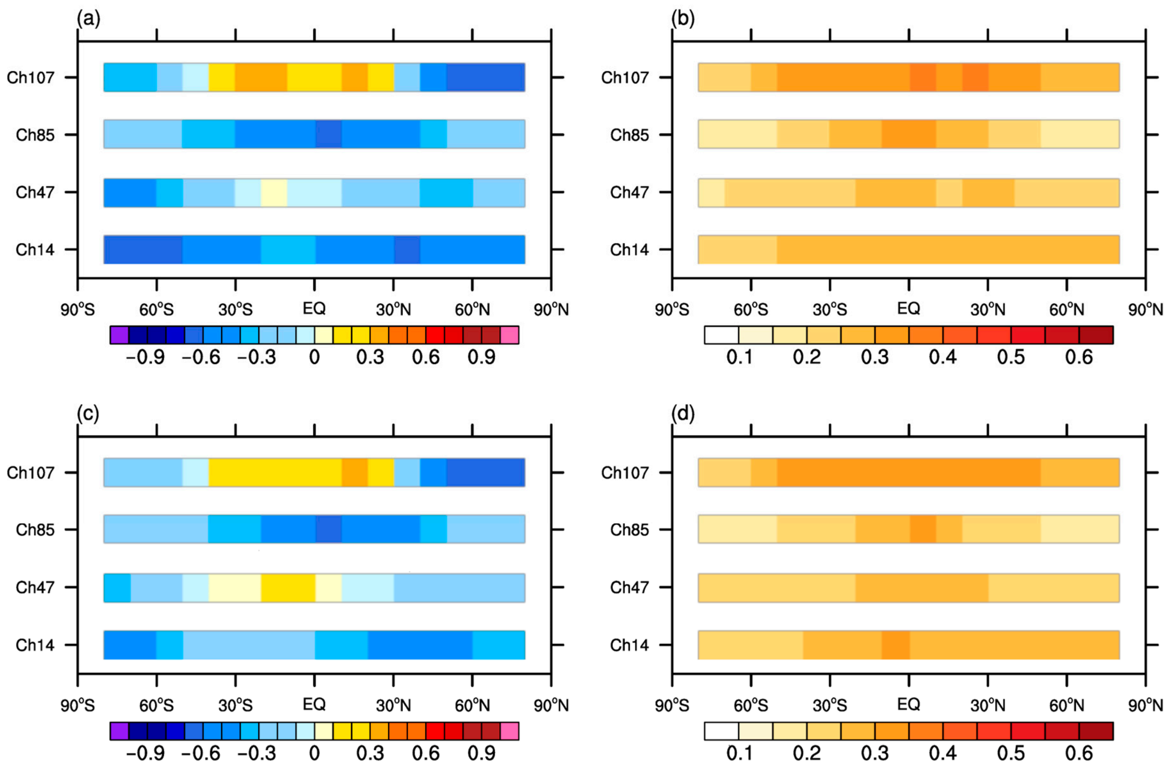

Figure 12. Statistical biases (**a**,**c**) and standard deviations (**b**,**d**) of channels 14, 47, 85, and 107 in 10° intervals of latitude during the (**a**,**b**) ascending and (**c**,**d**) descending orbit phases of HIRAS-II.

5. Conclusions

With the characteristics of high spectral and spatial resolutions, the observations of HIRAS-II can provide information on the atmospheric temperature and humidity in detail. In this paper, we analyze the O-B bias characteristics in the LW CO_2 channels of HIRAS-II over the clear-sky ocean. Before the bias analysis, the data were collected on apodization, cloud detection, and quality control. The comparison results of the quality-controlled pixels with the brightness temperature in the window channel show that the cloud-contaminated observations were effectively eliminated, and the O-Bs of the clear-sky observations meet the data preprocessing and quality control requirements. Subsequently, the influence of the FOV consistency, scanning position of FOR, diurnal variation in data, latitude, and the status of ascending and descending orbits on O-B was analyzed. The main conclusions are as follows:

(1) The O-B bias of the selected LW spectrum is between ± 1.0 K, except for the absorption peak, and the standard deviations of FOV1, FOV2, FOV4, FOV5, and FOV7 are stable and change little with the spectrum. The standard deviation of all FOVs is the closest, and the value is the smallest in the 670.625~705 cm^{-1} spectral band, which is less than 0.4 K (excluding FOV9).
(2) The O-B biases between the FOV4, FOV5, and other FOVs have good consistency within the LW spectral range; the biases of FOV1, FOV2, and other FOVs show secondary consistency.
(3) The bias variation trends in the stratospheric channels are consistent with the change in FOR, and the biases of the tropospheric channels on both sides of the scan line are greater than those of the stratosphere channels. The biases of FOV1 and FOV4 change little with the scanning positions, and the biases of FOV2 and FOV5 in the tropospheric channels change monotonically with the increase in the scanning points, but the change amplitudes are smaller than those of other FOVs.
(4) The differences in O-Bs among the LW channels during the day, the line of dawn and dusk, and night are small, and the changes are relatively similar. The difference in the standard deviations of O-Bs in the three cases is less than 0.1 K. The O-Bs of two typical channels (channels 14 and 47) in the stratosphere have disturbances at a few times, whereas the O-Bs are much more stable in time series in the tropospheric channels. The standard deviations of the O-Bs in the four channels are basically unchanged with time and stable within 0.4 K.
(5) The O-Bs of different channels show the characteristics of changing with the latitude band, the standard deviations of O-B is greater at low latitudes than at high latitudes. The negative biases of upper channels 14 and 47 in the descending orbit stage are generally smaller than those in the ascending stage, while the bias differences of tropospheric channels 85 and 107 between the ascending and descending orbits are small and less than 0.1 K. The standard deviations of O-Bs between the ascending and descending orbits are not much different.

Author Contributions: Conceptualization, J.H.; methodology, J.H. and G.M.; software, J.H. and G.L.; validation, J.H.; formal analysis, J.H. and G.M.; investigation, J.H., J.L. and H.Z.; data curation, G.L.; writing—original draft preparation, J.H. and G.M.; writing—review and editing, J.H. and G.M. All authors have read and agreed to the published version of the manuscript.

Funding: This research was supported by the National Key Research and Development Program of China (2022YFC3004002) and the Special Fund for Scientific Research (Meteorology) in the Public Interest of China (GYHY201506022).

Data Availability Statement: All data used in this paper are available from the authors upon request (huangj@cma.gov.cn).

Acknowledgments: The authors would like to acknowledge the National Satellite Meteorological Centre of CMA for providing the satellite data.

Conflicts of Interest: The authors declare no conflict of interest.

References

1. Eyre, J.R.; Bell, W.; Cotton, J.; English, S.J.; Forsythe, M.; Healy, S.B.; Pavelin, E.G. Assimilation of satellite data in numerical weather prediction. Part II: Recent years. *Q. J. R. Meteorl. Soc.* **2022**, *148*, 521–556. [CrossRef]
2. Bauer, P.; Thorpe, A.; Brunet, G. The quiet revolution of numerical weather prediction. *Nature* **2015**, *525*, 47–55. [CrossRef] [PubMed]
3. Eyre, J.R.; English, S.J.; Forsythe, M. Assimilation of satellite data in numerical weather prediction. Part I: The early years. *Q. J. R. Meteor. Soc.* **2019**, *146*, 49–68. [CrossRef]
4. Bormann, N.; Lawrence, H.; Farnan, J. Global Observing System Experiments in the ECMWF Assimilation System. ECMWF Technical Memorandum 839. 2019. Available online: https://www.ecmwf.int/sites/default/files/elibrary/2019/18859-global-observing-system-experiments-ecmwf-assimilation-system.pdf (accessed on 10 September 2023).
5. Menzel, W.P.; Schmit, T.J.; Zhang, P.; Li, J. Satellite-Based Atmospheric Infrared Sounder Development and Applications. *Bull. Amer. Meteor. Soc.* **2018**, *99*, 583–603. [CrossRef]
6. Chahine, M.T.; Pagano, T.S.; Aumann, H.H.; Atlas, R.; Barnet, C.; Blaisdell, J.; Chen, L.; Divakarla, M.; Fetzer, E.J.; Goldberg, M.; et al. AIRS: Improving weather forecasting and providing new data on greenhouse gases. *Bull. Amer. Meteor. Soc.* **2006**, *87*, 911–926. [CrossRef]
7. Klaes, K.D.; Cohen, M.; Buhler, Y.; Schluessel, P.; Munro, R.; Luntama, J.P.; Von Engelin, A.; Clerigh, E.O.; Bonekamp, H.; Ackermann, J.; et al. An Introduction to the EUMETSAT Polar system. *Bull. Amer. Meteor. Soc.* **2007**, *88*, 1085–1096. [CrossRef]
8. Noh, Y.C.; Huang, H.L.; Goldberg, M.D. Refinement of CrIS Channel Selection for Global Data Assimilation and Its Impact on the Global Weather Forecast. *Weather. Forecast.* **2021**, *36*, 1405–1429. [CrossRef]
9. Wu, C.Q.; Qi, C.L.; Hu, X.Q.; Gu, M.J.; Yang, T.H.; Xu, H.L.; Lee, L.R.; Yang, Z.D.; Zhang, P. FY-3D HIRAS Radiometric Calibration and Accuracy Assessment. *IEEE Trans. Geosci. Remote Sens.* **2020**, *99*, 1–12. [CrossRef]
10. Yang, J.; Zhang, Z.; Wei, C.; Lu, F.; Guo, Q. Introducing the New Generation of Chinese Geostationary Weather Satellites, Fengyun-4. *Bull. Amer. Meteor. Soc.* **2017**, *98*, 1637–1658. [CrossRef]
11. Aumann, H.H.; Chahine, M.T.; Gautier, C.; Goldberg, M.D.; Kalnay, E.; McMillin, L.M.; Revercomb, H.; Rosenkranz, P.W.; Smith, W.L.; Staelin, D.H.; et al. AIRS/AMSU/HSB on the Aqua mission: Design, science objectives, data products, and processing systems. *IEEE Trans. Geosci. Remote Sens.* **2003**, *41*, 253–264. [CrossRef]
12. Wang, X.; Zou, X. Quality Assessments of Chinese FengYun-3B Microwave Temperature Sounder (MWTS) Measurements. *IEEE Trans. Geosci. Remote Sens.* **2012**, *50*, 4875–4884. [CrossRef]
13. Lu, Q.; Bell, W.; Bauer, P.; Bormann, N.; Peubey, C. An evaluation of FY-3A satellite data for numerical weather prediction. *Q. J. R. Meteorol. Soc.* **2011**, *137*, 1298–1311. [CrossRef]
14. Amato, U.; Cuomo, V.; Rizzi, R.; Serio, C. Evaluating the effect of the inter-relationships among the different spectral bands on IASI performance. *Q. J. R. Meteor. Soc.* **1997**, *123*, 2231–2244. [CrossRef]
15. Le Marshall, J.; Jung, J.; Derber, J.; Chahine, M.; Treadon, R.; Lord, S.J.; Goldberg, M.; Wolf, W.; Liu, H.C.; Joiner, J.; et al. Improving Global Analysis and Forecasting with AIRS. *Bull. Amer. Meteor. Soc.* **2006**, *87*, 891–895. [CrossRef]
16. Hilton, F.; Atkinson, N.C.; English, S.J.; Eyre, J.R. Assimilation of IASI at the Met Office and assessment of its impact through observing system experiments. *Q. J. R. Meteorl. Soc.* **2009**, *135*, 495–505. [CrossRef]
17. Zhang, P.; Lu, Q.F.; Hu, X.Q.; Gu, S.Y.; Yang, L.; Min, M.; Chen, L.; Xu, N.; Sun, L.; Bai, W.G.; et al. Latest Progress of the Chinese Meteorological Satellite Program and Core Data Processing Technologies. *Adv. Atmos. Sci.* **2019**, *36*, 1027–1045. [CrossRef]
18. Qi, C.L.; Wu, C.Q.; Hu, X.Q.; Xu, H.; Lee, L.; Zhou, F.C.; Gu, M.G.; Yang, T.H.; Shao, C.Y.; Yang, Z.D.; et al. High Spectral Infrared Atmospheric Sounder (HIRAS): System Overview and On-Orbit Performance Assessment. *IEEE Trans. Geosci. Remote Sens.* **2020**, *58*, 4335–4352. [CrossRef]
19. Carminati, F.; Xiao, X.; Lu, Q.; Atkinson, N.; Hocking, J. Assessment of the Hyperspectral Infrared Atmospheric Sounder (HIRAS). *Remote Sens.* **2019**, *11*, 2950. [CrossRef]
20. Zhang, P.; Hu, X.Q.; Lu, Q.F.; Zhu, A.J.; Lin, M.Y.; Sun, L.; Chen, L.; Xu, N. FY-3E: The first operational meteorological satellite mission in an early morning orbit. *Adv. Atmos. Sci.* **2021**, *39*, 1–8. [CrossRef]
21. Yang, T.H.; Gu, M.J.; Shao, C.Y.; Wu, C.Q.; Qi, C.L.; Hu, X.Q. Nonlinearity correction of FY-3E HIRAS-II in pre-launch thermal vacuum calibration tests. *J. Infrared Millim. Waves.* **2022**, *41*, 597–607. [CrossRef]
22. Zhang, C.; Qi, C.; Yang, T.; Gu, M.; Zhang, P.; Lee, L.; Xie, M.; Hu, X. Evaluation of FY-3E/HIRAS-II Radiometric Calibration Accuracy Based on OMB Analysis. *Remote Sens.* **2022**, *14*, 3222. [CrossRef]
23. Chen, D.H.; Xue, J.S.; Yang, X.S.; Zhang, H.L.; Shen, X.S.; Hu, J.L.; Wang, Y.; Ji, L.R.; Chen, J.B. New generation of multi-scale NWP system (GRAPES): General scientific design. *Chin. Sci. Bull.* **2008**, *53*, 3433–3445. [CrossRef]
24. Xue, J.S.; Zhuang, S.Y.; Zhu, G.F.; Zhang, H.; Liu, Z.Q.; Liu, Y.; Zhuang, Z.R. Scientific design and preliminary results of three-dimensional variational data assimilation system of GRAPES. *Chin. Sci. Bull.* **2008**, *53*, 3446–3457. [CrossRef]
25. Zhang, L.; Liu, Y.; Liu, Y.; Gong, J.; Lu, H.; Jin, Z.; Tian, W.; Liu, G.; Zhou, B.; Zhao, B. The operational global four-dimensional variational data assimilation system at the China Meteorological Administration. *Q. J. R. Meteorol. Soc.* **2019**, *145*, 1882–1896. [CrossRef]
26. Saunders, R.; Hocking, J.; Turner, E.; Rayer, P.; Rundle, D.; Brunel, P.; Vidot, J.; Roquet, P.; Matricardi, M.; Geer, A.; et al. An update on the RTTOV fast radiative transfer model (currently at version 12). *Geosci. Model Dev.* **2018**, *11*, 2717–2737. [CrossRef]

27. Li, X.; Zou, X.L. Bias characterization of CrIS radiances at 399 selected channels with respect to NWP model simulations. *Atmos. Res.* **2017**, *196*, 164–181. [CrossRef]
28. McNally, A.P.; Watts, P.D. A cloud detection algorithm for high-spectral-resolution infrared sounders. *Q. J. R. Meteorol. Soc.* **2003**, *129*, 3411–3423. [CrossRef]
29. Goldberg, M.D.; Qu, Y.; McMillin, L.M.; Wolf, W.; Zhou, L.H.; Divakarla, M. AIRS near-real-time products and algorithms in support of operational numerical weather prediction. *IEEE Trans. Geosci. Remote Sens.* **2003**, *41*, 379–389. [CrossRef]
30. Collard, A.D.; McNally, A.P. The assimilation of Infrared Atmospheric Sounding Interferometer radiances at ECMWF. *Q. J. R. Meteorol. Soc.* **2009**, *135*, 1044–1058. [CrossRef]
31. McNally, A.P.; Watts, P.D.; Smith, A.J.; Engelen, R.; Kelly, G.A.; Thépaut, J.N.; Matricardi, M. The assimilation of AIRS radiance data at ECMWF. *Q. J. R. Meteorol. Soc.* **2006**, *132*, 935–957. [CrossRef]
32. Deng, S.; Li, G.; Zhang, H. Objective Determination scheme of Threshold in High-spectral-resolution infrared cloud detection. *Meteorol. Mon.* **2017**, *43*, 213–220.
33. Harris, B.A.; Kelly, G. A satellite radiance-bias correction scheme for data assimilation. *Q. J. R. Meteorol. Soc.* **2001**, *127*, 1453–1468. [CrossRef]
34. Liu, Z.Q.; Zhang, F.Y.; Wu, X.B.; Xue, J.H. A regional atovs radiance-bias correction scheme for rediance assimilation. *Acta Meteorol. Sin.* **2007**, *1*, 113–123. [CrossRef]